ARTICLE

Microwave-assisted synthesis followed by a reduction step: making persistent phosphors with a large storage capacity

Received 00th January 20xx,
Accepted 00th January 20xx

DOI: 10.1039/x0xx00000x

José Miranda de Carvalho,[a,b,*] David Van der Heggen,[a] Lisa I.D.J. Martin,[a] Philippe F. Smet[a]

The performance of impurity doped luminescent materials, or phosphors, depends on the composition and crystallinity of the host compound, as well as on the distribution and valence state of the dopant ions. This is particularly true for persistent phosphors, where both luminescence centers and charge trapping defects are required. Here we show that splitting the synthesis procedure in two separate steps offers a simple way to obtain efficient persistent phosphors which are superior to phosphors prepared *via* a conventional solid state synthesis using a single step. The storage capacity of the persistent phosphor benefits from using a microwave assisted solid state synthesis (MASS) to achieve superior compositional homogeneity, followed by a short heat treatment in reducing atmosphere to reduce the activators. In this work, the approach is demonstrated for the efficient blue-emitting Eu^{2+},Dy^{3+} co-doped $Sr_2MgSi_2O_7$ persistent phosphor. The enhanced ionic diffusion during the MASS not only improves the homogeneity and dopant distribution, but also allows to obtain the phosphor in considerably shorter times (*ca.* 25 minutes). The storage capacity of the as-obtained phosphors prepared by MASS is slightly higher than those obtained by the conventional solid-state method. Cathodoluminescence (CL) measurements evidenced however the existence of a large fraction of unreduced europium activators. Using a short reducing step at 900°C, the Eu^{3+} emission was almost fully suppressed in CL and as a consequence, the storage capacity of the MASS-obtained material showed a ten fold increase, confirming the benefit of decoupling compositional homogeneity and the dopant reduction step for phosphor synthesis.

Introduction

The search for new advanced solid-state materials in the past few decades is becoming stronger due to the necessity of more efficient batteries,[1] capacitors,[2] memory,[3] and lighting devices.[4–13] Although solid materials can be obtained by a variety of methods, such as conventional solid-state (CSS) synthesis,[14] combustion synthesis,[15] or sol-gel methods,[16] the CSS method is by far the most widely used. Combining the easy-to-process method allied with the low number of steps grants high reproducibility and is responsible for the high popularity of the CSS method. In the CSS method, usually performed at a high-temperature, direct reaction is expected where all the solid reactants, with different grain sizes and randomly oriented surfaces, must react through ionic diffusion in order to form the product at the interface of two grains. The most common drawback of the solid-state reactions is the limited flux of diffusing species of precursors hindering the process of crystal growth and therefore the formation of the final products.

The microwave-assisted solid-state (MASS)[17,18] synthesis is receiving more attention nowadays as an alternative way to obtain advanced solid-state materials. Literature has proven that the MASS method is efficient to obtain oxides,[7,19] aluminates,[20] silicates,[21] oxysulfides,[22] and minerals[23]. However, the MASS synthesis is still not fully understood and lacking the procedure for several class of materials, such as the persistent luminescence ones. MASS synthesis is proven to be a faster way to obtain solid-state materials, in a matter of minutes rather than hours.[17] It is considered a greener, more cost-effective method due to the lower thermal input. However, the most important reason to use microwave irradiation in solid-state syntheses is to overcome the diffusion limits in solids. It has been demonstrated that microwave fields can exert ponderomotive forces and consequently increase the solid-state ionic diffusion.[24] Therefore, microwave irradiation offers the opportunity to reduce processing times and improve the material's properties if carefully selected conditions of irradiation are chosen. Also, when intentional impurities (dopants) are added to the material's precursor, it is expected to disperse them more homogeneously into the crystal. The enhanced diffusivity of the species in the solids can increase the homogeneity of the final materials significantly, providing highly crystalline and well-formed materials.[25] Despite the growing interest of the scientific community, the MASS synthesis is still not fully understood and lacking the procedure for several class of materials, such as the persistent luminescence ones.

Persistent luminescence (PeL) is observed when the emitting ion, often Eu^{2+}, is excited by radiation (UV-VIS, or X-rays)

[a] *Lumilab, Department of Solid-State Sciences, Ghent University, Krijgslaan 281, S1, 9000 Gent, Belgium.*
[b] *Institute of Physics, University of São Paulo, BR-05508-900, São Paulo-SP, Brazil.*
Electronic Supplementary Information (ESI) available: [details of any supplementary information available should be included here]. See DOI: 10.1039/x0xx00000x

followed by delocalization of a charge carrier.[26] These charge carriers are eventually trapped by defects and form long-lived states in the crystalline structure.[27–30] After absorption of available thermal (*k*T) or optical (*h*ν) energy, the trapped electron can recombine with the emitting centre and emit light.[31] Eu^{2+}, Dy^{3+} co-doped $Sr_2MgSi_2O_7$ materials show blue PeL (λ_{max}: 470 nm) after removal of the excitation source in the UV-region (365 nm). It is assumed that the trapping of the charge carrier occurs at intrinsic or extrinsic defects in the crystal, such as oxygen vacancies, or co-dopants such as Dy^{3+}. The Eu^{2+} doped materials are the most investigated for PeL and most of the benchmark materials for PeL in the visible spectrum have Eu^{2+} as emitting center.[26,32]

In this work, we compare the persistent luminescence properties of the $Sr_2MgSi_2O_7:Eu^{2+},Dy^{3+}$ obtained by both CSS and MASS methods in a systematic fashion. The materials were fully characterized and compared with the commercial $Sr_2MgSi_2O_7:Eu^{2+},Dy^{3+}$ blue PeL material.

Experimental

Syntheses details

Different samples were produced using either the conventional (CSS) or the microwave-assisted solid-state (MASS) method. Both synthesis methods start from the same precursor mixture, which was prepared by thoroughly mixing and grinding the stoichiometric amounts of $SrCO_3$ (Sigma-Aldrich, 99.5 %), $(MgCO_3)_4.Mg(OH)_2$ (Sigma-Aldrich, 99%), SiO_2 (Sigma-Aldrich, > 99.9 %), Eu_2O_3, and Dy_2O_3 (CSTARM, 99.99 %), in an alumina mortar to obtain the final composition $Sr_2MgSi_2O_7:xEu^{2+},yDy^{3+}$ with x = 1 mole-%, and y = 1, 3, and 10 mole-%.

The conventional solid-state (CSS) method followed previously reported syntheses.[33,34] For a standard procedure, approximately 1 g of the material was placed in an alumina boat and inserted in a tube furnace and heated at 1250 °C for 4 hours. The temperature was raised using a constant heating rate of 5 °C/min in a dynamic reducing atmosphere with composition H_2(10%)/N_2(90%), flowing at a constant rate of 200 mL/min.

The microwave-assisted solid-state (MASS) synthesis was based on an adjusted protocol described previously.[19,22] In a typical synthesis, *ca.* 0,5 g of the precursor mixture was placed in a 5 mL alumina crucible. The 5 mL crucible was pushed into a 35 mL alumina crucible containing 10 g of activated carbon in order to be surrounded by the susceptor. Both crucibles were covered with an alumina disc and inserted in an aluminosilicate brick used as thermal insulation. The mounted setup is inserted in a domestic microwave oven and irradiated during12 minutes at 1000 W, followed by 10 minutes at 900 W. After the irradiation the material was allowed to cool to room temperature. The program was chosen after several trials to achieve the reproducibility of the final temperature of the carbon (1250 °C) measured with a hand-pyrometer (Trotec, TP10). The temperature profile has an asymptotic behavior as usually observed for microwave heating processes with a steep heating rate at the beginning of the curve and finally achieving a plateau temperature when reaching thermal equilibrium.[22]

Because most of the ceramic materials interact weakly with the microwave radiation, the MASS synthesis needs a susceptor[35] to absorb the electromagnetic radiation and convert it to heat at the beginning of the process. For the studied materials, activated carbon (Ø: 1–2 mm, Sigma-Aldrich) was used to initiate the heating and generate CO gas *in situ* by incomplete burning.

Characterization

The phase purity of all the prepared powders was checked using X-ray diffraction (XRD), utilizing CuK_α radiation (λ: 1.5406 Å) on a Siemens D5000 diffractometer (40 kV, 40 mA). The XRD patterns were fitted using the GSAS EXPGUI program suite,[36] with Rietveld code for structural model fit.

Scanning electron microscopy was performed in a Hitachi S-3400 N, equipped with a ThermoScientific Noran System 7 for energy-dispersive X-ray (EDX) analysis. Cathodoluminescence was captured with an Acton SP2300 monochromator and ProEM 1600 EMCCD camera, both from Princeton Instruments, leading to hyperspectral CL maps. All EDX and CL measurements were performed with a beam energy of 20 keV and at a pressure of 20 Pa to avoid excessive charging of the samples.

The photoluminescence (PL) of the materials was studied using an Edinburgh FS920 (Edinburgh Instruments Ltd.) fluorescence spectrometer with a monochromated 450 W Xe-arc lamp as the excitation source.

Quantum yield was measured using a $BaSO_4$ coated sphere apparatus with a 375 nm LED excitation source. The emission was recorded using a ProEM1600 EMCCD camera attached to an Acton SP2300 monochromator. The sphere was calibrated using a commercial phosphor emitting in a similar range ($BAM:Eu^{2+}$, QY: 90%).

Luminance measurements were performed using an ILT 1700 calibrated photometer (International Light Technologies) equipped with a photopic filter (YPM). The samples were placed on a diffuse reflective $BaSO_4$-coated sample holder to enable detection of the light emitted in all directions. The photon counting experiment was performed according to previously reported methodology.[37] The measurements were performed with the phosphor dispersed in a silicone polymer layer (Silgard 184). The layer is produced using a mixture with a 10:1:0.1 weight proportion of elastomer:catalyst:phosphor that is deposited on the top of a microscope glass slide. The polymer is dried in a muffle at 50 °C for 1 h. After that, the phosphor-containing polymer is removed from the glass slide and cut into a circle with a 2.54 cm^2 area.

The TL setup consists of an excitation source (375 nm LED), a cooling and heating stage (-60 to +225°C) and a fiber-based emission detection using a ProEM1600 EMCCD camera attached to an Acton SP2300 monochromator, from Princeton Instruments. All components are software controlled, allowing a high reproducibility in measurements and extended measurement cycles probing a large part of the full parameter space.

Results and discussion

Structure, morphology, and dopant distribution

All the $Sr_2MgSi_2O_7$:Eu^{2+}, Dy^{3+} materials obtained by conventional (CSS) and microwave-assisted solid-state (MASS) syntheses mainly consist of the melilite-type tetragonal structure (space group: $P\bar{4}2_1m$; PDF #01-075-1736)[38] by the XRD patterns (**Fig. 1, top**). The melilite tetragonal structure is composed of a sheet of linked tetrahedra (Si_2O_7 and MgO_4) connected by an interlayer of Sr^{2+} cations (**Fig. 1, bottom**). The strontium cations occupy a distorted antiprismatic polyhedron with an 8-coordination environment having a low-symmetrical point group (C_s). The Sr^{2+} site is advantageous to Eu^{2+}-doping due to the small difference in their ionic radii (r_{eff}(Sr^{2+}): 1.26 Å, r_{eff} (Eu^{2+}): 1.25 Å; C.N.: 8).[39]

The main crystalline impurities observed in the materials are the $Sr_3MgSi_2O_8$ and Sr_2SiO_4 phases indicating Mg segregation from the original stoichiometry, which will cause local discrepancies in the Mg/Si ratio.[21] Increasing the concentration of Dy^{3+} co-dopant contributes to higher levels of impurities in both methods. The formation of impurities is most probably related to the clustering of the Dy^{3+} ions that facilitate the formation of segregated phases, due to the charge mismatch between Sr^{2+} and Dy^{3+}.

It was observed by SEM-EDX (**Fig. S1, ESI**) that segregations for high concentrations of Dy^{3+} were mostly forming intergrain aggregates or completely separate particles or microrods with a composition close to MgO-Dy_2O_3.

The Eu^{2+} ions are expected to easily substitute for the Sr^{2+} ions, as they have the same valence state and almost the same ionic size[39,40]. The Sr^{2+} site (x: 0.3345, y: 0.1655, z: 0.5070) in the $Sr_2MgSi_2O_7$ features an 8-coordinated environment with oxygen atoms, with average Sr-O bond length of 2.6717 Å. Consequently, no segregation of the Eu ions is expected for the moderate doping concentration of 1 mole-%. On the other hand, the radius of the Dy^{3+} ion is *ca.* 19% smaller than the one of Sr^{2+} (r_{eff} (Dy^{3+}): 1.027 Å; C.N.: 8), which can limit the amount of co-doping and increase the probability of segregation for high concentrations.

The Rietveld structural analysis shows shrinkage in the lattice parameters (*a* and *c*) for the doped materials obtained by both methods (**Fig. 2**, **center and right**). This behavior was already expected since the Dy^{3+} dopant has a smaller ionic radius than Sr^{2+}. As the concentration of Dy^{3+} increases, the lattice parameter *c* continues to shrink, whereas a small increase in the parameter *a* is observed. The increase in *ab* plane is due to the proximity of the magnesium-silicate planes that causes electrostatic repulsion of the MgO_4-Si_2O_7 groups with the intercalated SrO_8.[41–43] As a result, the elongation of the average MgO_4 and Si_2O_7 bonds is necessary to minimize the repulsion, leading to elongation in the *ab* plane. The *a*/*c* ratio corroborates with the interpretation, indicating a higher compression rate between MgO_4-Si_2O_7 planes with the increasing of Dy^{3+} concentration. The effective packing is also increasing with the Dy^{3+} concentration, which is in accordance

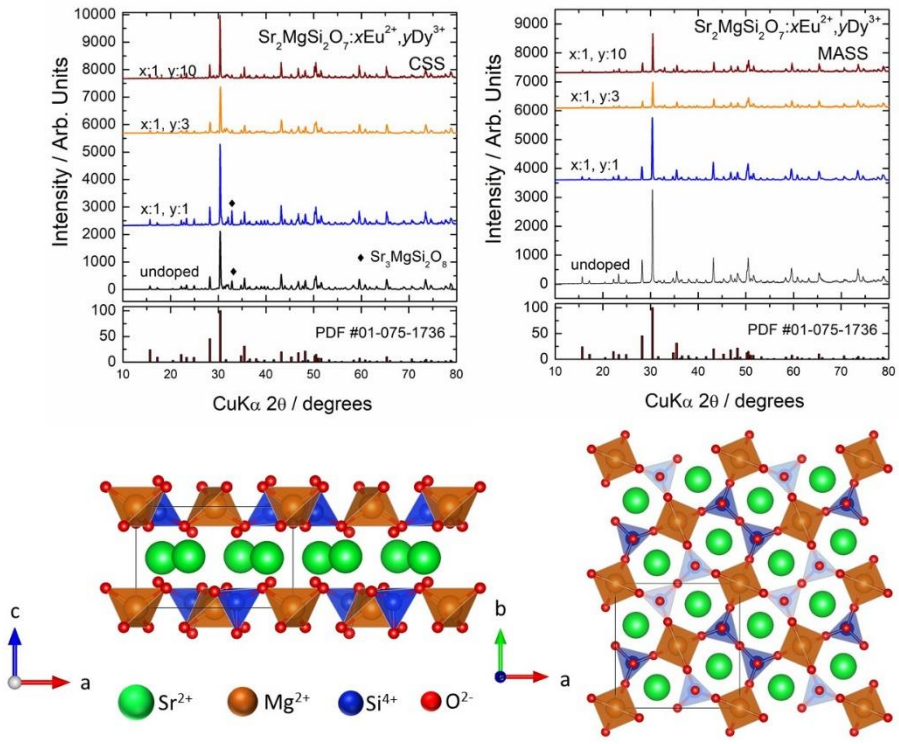

Figure 1. X-ray powder diffraction of the $Sr_2MgSi_2O_7$:Eu^{2+},Dy^{3+} materials obtained by both conventional (CSS, top left) and microwave-assisted (MASS, top right) methods with different concentration of Dy^{3+} co-dopant. VESTA[52] representation of the melilite-type structure (PDF #01-075-1736) viewed along the *a* (bottom left), and *c* (bottom right) axis is also provided.

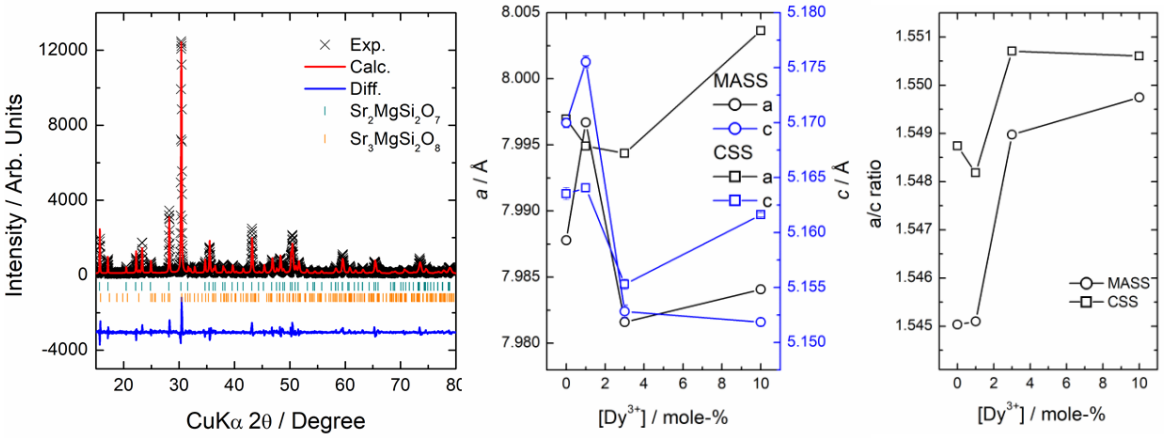

Figure 2. Exemplary Rietveld plot (left) of the non-doped $Sr_2MgSi_2O_7$ material obtained by the MASS method. Calculated lattice parameters (*a*, and *c*) for all the different co-dopant concentrations (center) and the *a*/*c* compression ratio (right) is showed for both MASS and CSS methods. The error bars for the lattice parameters are smaller than the symbols in the image.

with the average doping site for the materials being indeed the Sr^{2+} sites.[42,43]

The lattice parameters for the CSS-obtained materials decrease as function of the Dy^{3+} concentrations. However, for high concentrations of Dy^{3+} (10 mole-%), both *a* and *c* lattice parameters indicate an elongation, that can be interpreted as poorer incorporation of Dy^{3+} in the crystal when comparing with the MASS-obtained materials. Similarly, the *a*/*c* ratio indicates a higher compression factor for the MASS-obtained materials showing that the microwave irradiation promotes a better average incorporation of Dy^{3+} in the crystals, even if the synthesis time is much shorter than for the CSS method.

The morphology of the materials was studied using scanning electron microscopy (SEM), and it was observed that the different methods yield materials with different microstructure. The non-doped $Sr_2MgSi_2O_7$ material obtained by the CSS method has well-sintered aggregated round particles that grow by coalescence of small particles (**Fig. 3, a and b**). The particle coalescence process in the CSS synthesis is governed mainly by thermal energy, leading to isotropic growth. The particle size distribution is composed of large micrometric sized particles with fewer sub-micrometric particles that are in accordance with the Ostwald ripening where large particles grow at the expense of the smaller ones.[44] The non-doped $Sr_2MgSi_2O_7$ material obtained by the MASS method has well-defined angular-edged particles composed by a layered structure that are stacked onto each other (**Fig. 3**, **c and d**). The stacked microstructure of the non-doped material obtained by the MASS method agrees with the crystalline structure of the melilite-type mineral, which has a layered magnesium-silicate structure. It was also observed that micrometric rods are present in the material obtained by MASS method (**Fig. 3, d, yellow arrows**). The microrods' chemical composition was assessed using SEM-EDX mapping, confirming that a phase is formed with the approximate atomic ratio of 2:1:2, for Sr, Mg, and Si, respectively (**Fig. S2, ESI**). The presence of microrods in the microwave-assisted solid-state process without using structural templates was already reported for different materials, *e.g.*, β-SiC[45], and β-$NaYF_4$.[46] It is attributed mainly to the particle growing mechanism that starts with the formation of nanocrystals leading to the micrometric structure in a swift process.

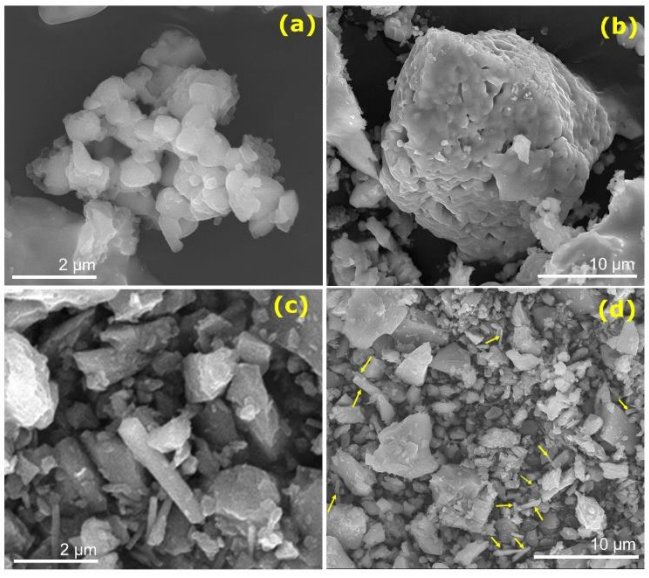

Figure 3. SEM images of the non-doped $Sr_2MgSi_2O_7$ obtained by conventional (a, b) and microwave-assisted (c, d) solid-state methods. The yellow arrows point at the microrods formed during the MASS synthesis.

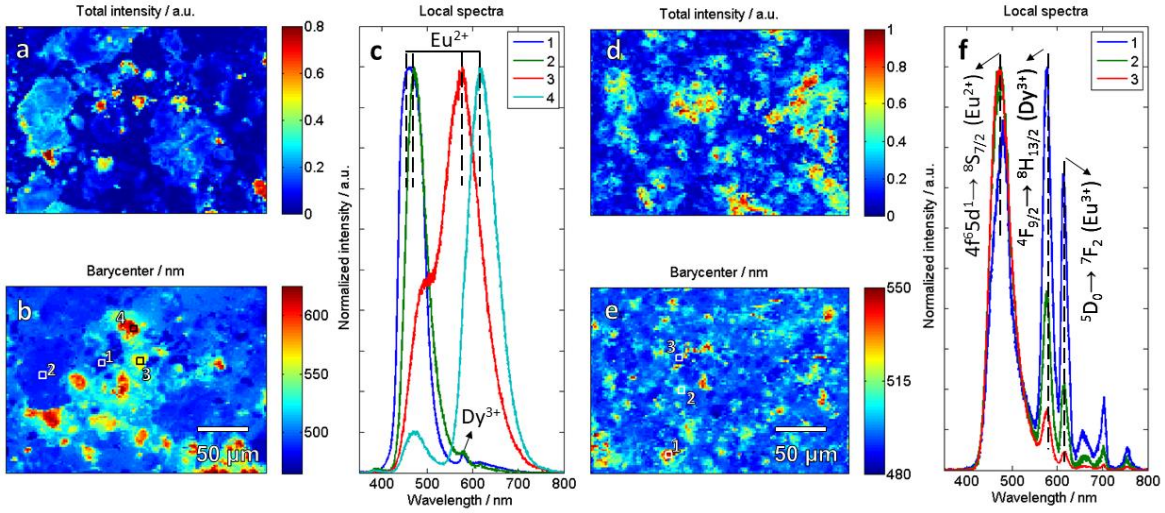

Figure 4. SEM-CL hyperspectral images of the $Sr_2MgSi_2O_7$:Eu^{2+}(1%),Dy^{3+}(1%) materials obtained by CSS (a, b) and MASS (d, e) method. The numbers in the images (b, and e) correspond to the area of the local spectra extracted for the CSS (c) and MASS (f) materials.

Local analysis of Eu^{2+} cathodoluminescence emission in $Sr_2MgSi_2O_7$

Since the chemical composition is directly related to the optical properties of the phosphors, combined SEM-CL-EDX analysis is a powerful tool to assess the homogeneity of the materials at the microscopic level.[25] The Eu^{2+} ion is very sensitive to the chemical environment that will generate different crystal fields and subsequently different splitting of the 5d energy levels, resulting in varied emission colors. For the case of the SrO-MgO-SiO_2 system, the variation of the Mg/Sr ratio can lead to the local formation of $Sr_3MgSi_2O_8$, generating bluish (peaking at 455 nm) emission of Eu^{2+}. Also, local Mg absence can result in the formation of a Sr_2SiO_4 phase, which presents a greenish-yellow emission band (560 nm). In order to investigate the compositional and spectral properties on a microscopic level, we performed SEM-CL-EDX spectral imaging. **Figure 4** shows the cathodoluminescence maps for the samples obtained by the CSS and MASS methods, both with the same nominal concentration of Eu and Dy ions (1 mole-% related to Sr^{2+}). The CL emission of the CSS-obtained material (**Fig. 4**, **a-c**) has an inhomogeneous local CL emission profile throughout the selected areas. The barycenter of the emission spectrum in the CSS-obtained sample varies in the range of 450 to 625 nm indicating a wide gamut of emitting colours and consequently Eu^{2+} ions emitting from multiple different crystalline sites. CL local emission bands can be attributed to Eu^{2+} doped $Sr_3MgSi_2O_8$ (λ_{max}: 457 nm), $Sr_2MgSi_2O_7$ (λ_{max}: 470 nm) and, Sr_2SiO_4 (λ_{max}: 560 nm), reflecting inhomogeneities in the Mg/Si ratio. These mentioned impurities are in accordance with the ones observed in the XRD analysis.

On the other hand, CL emission from the MASS-obtained material has a remarkably homogeneous local emission with only one broadband emission, with maximum at *ca*. 470 nm, attributed to the $4f^65d^1 \rightarrow 4f^7$ ($^8S_{7/2}$) transition of Eu^{2+} diluted in the $Sr_2MgSi_2O_7$ host. The CL spectra of the MASS sample also show the Dy^{3+} ($^4F_{9/2} \rightarrow {}^6H_{13/2}$; 574 nm) and Eu^{3+} ($^5D_0 \rightarrow {}^7F_2$; 615 nm) narrow *f-f* emission bands. The mean barycenter of the observed area is close to 490 nm, and it is varying only due to the different ratio between the broadband Eu^{2+} emission at 470nm and the sharp emission bands of Eu^{3+} and Dy^{3+} in the range from 550 to 750 nm. The presence of Eu^{3+} emission in the cathodoluminescence for MASS-obtained material indicates an incomplete reduction of the ion in the CO atmosphere during the MASS synthesis.

SEM-CL analysis confirms a variety of local emitting sites of europium in the CSS samples leading to an overall non-optimal optical behaviour. In comparison, the MASS-obtained material has a more homogeneous local cathodoluminescence emission, which is related to a homogeneous chemical composition at the microscopic level. Despite the fast nature of MASS synthesis, the combination of thermal and microwave irradiation effects grants the high homogeneity through enhancement of the diffusivity of the ions during the process. However, the MASS method described in this work is not providing the needed reducing atmosphere to sufficiently reduce the Eu^{3+} ion. It can be expected that a reducing step in mild temperature conditions would greatly favour the MASS-obtained phosphors, as will be discussed in **next sections**.

Optical properties of the Eu,Dy co-doped $Sr_2MgSi_2O_7$ materials

All the materials prepared by both MASS and CSS methods show a broad emission band, centred *ca.* 470 nm, attributed to Eu^{2+} *f-d* transitions (**Fig. 5, a**) when excited by a 375 nm LED. At room temperature, there are no contributions from *f-f* transitions from Dy^{3+} ions even in high concentrations regime. Also, Eu^{3+}

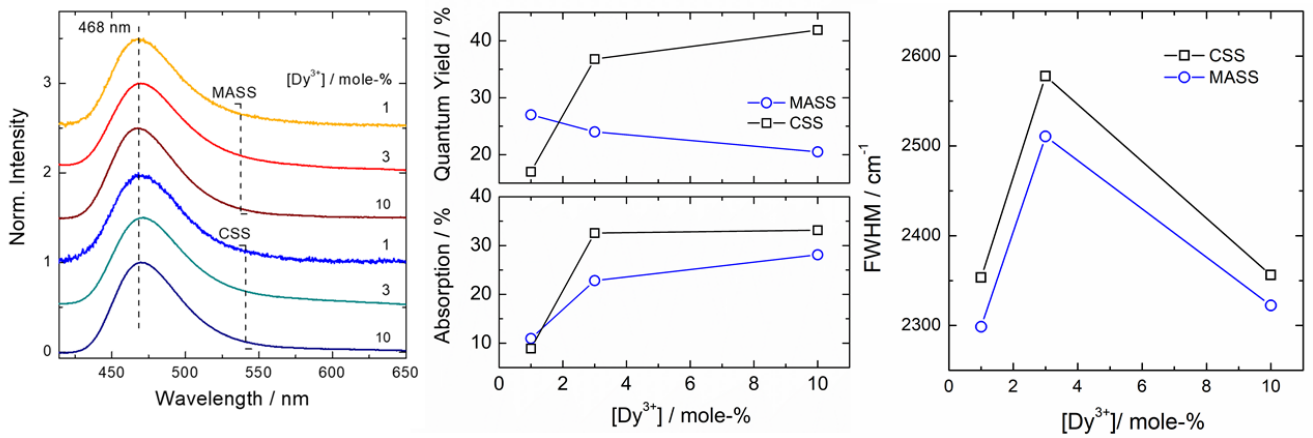

Figure 5. Room temperature PL spectra of Sr2MgSi2O7:Eu2+,Dy3+ for all studied Dy3+ concentrations, both MASS and CSS methods (a). Quantum yield and the absorption for all studied materials (b). FWHM of the emission band upon excitation at 365 nm for all studied samples (c).

ion *f-f* emissions are not detected using the conventional PL spectroscopy, as expected due to the high absorption of Eu^{2+} and the possibility of quenching *via* $Eu^{2+/3+}$ intevalence charge transfer.[47] Eu^{2+}-doped Sr-åkermanite has a broad emission band due to a splitting of the $4f^65d^1$ levels of Eu^{2+} ions occupying the Sr^{2+} position. In the $Sr_2MgSi_2O_7$ material, low symmetry of the distorted antiprismatic point structure (C_s) for europium ion leads to a very dense manifold of energy levels that give rise to a broad excitation band (*ca.* 10000 cm^{-1}).

The analysis of the emission band broadness (FWHM) can give an essential insight into the crystal field splitting for the Eu^{2+} ion. The emission band of all the materials obtained by both methods has a similar broadness ranging from 2300-2500 cm^{-1}. The obtained values are following literature for Eu^{2+} doped in Sr-åkermanites (2120 cm^{-1}).[48,49] The increase in co-dopant concentration to 3 mole-% of Dy^{3+} promotes an increase in the FWHM by almost 300 cm^{-1} in the emission bandwidth (**Fig. 5, c**). However, for the higher concentration case, excessive broadness is not observed. The broadness observed for the 3 mole-% of Dy^{3+} can be ascribed to three main reasons:

i) emission from secondary phases of the materials that might be overlapping with the emission of the $Sr_2MgSi_2O_7$ phase; *ii*) overlapping with *f-f* emissions from either Eu^{3+} or Dy^{3+} ions, and *iii*) the existence of non-equivalent sites for the Eu^{2+}. Also, MASS-obtained materials have narrower FWHM of the PL emission bands in comparison with the CSS-obtained ones, in accordance with the higher homogeneity already observed in the SEM-CL maps.

In order to compare the efficiency of the photoluminescence process of the materials in a quantitative way, the internal quantum yield (Φ) was calculated as follows:

$$\Phi = \frac{N_{\gamma,em}}{N_{\gamma,abs}} \qquad (3)$$

which is the ratio the total number of the photons emitted ($N_{\gamma,em}$) to the total number of photons absorbed ($N_{\gamma,abs}$) by the material. The quantum yield of the materials obtained by the MASS method decreases when the concentration of Dy^{3+} increases (**Fig. 5, b**). On the contrary, the absorption ($N_{\gamma,abs}$) is increasing considerably when the co-dopant concentration is increased. The reasons on the decrease in the quantum yield values in the MASS-obtained materials is not entirely clear, however, two main reasons can be cited: *i*) with the increase of the concentration of the Dy^{3+} co-dopants a higher number of process can be active, such as optical stimulated luminescence, which can reduce the quantum efficiency because it's a two-for-one process,[50] *ii*) microwave irradiation increase the diffusion of the ions that enhance the incorporation of Dy^{3+}, which subsequently creates more defects via charge compensation effects; Hence, the defects can act as killing centre after the absorption of the incident light, and *iii*) The presence of Eu^{2+}-Eu^{3+} pairs can act as quenching centres *via* intervalence charge transfer transition, as mentioned previously. The combination of these effects corroborates with the increase of the light absorption contribution and the hindering the quantum yield.

In comparison, the values for quantum yield for the CSS-obtained are increasing with the concentration of Dy^{3+} value to as high as 45% (10 mole-% Dy^{3+}). These values are more in accordance with those reported in literature[49] and the one found for the measured commercial $Sr_2MgSi_2O_7$:Eu^{2+} material (Φ = 40 %; λ_{exc}: 375 nm). The considerable difference between the two methods can be largely accounted by the incomplete reduction of Eu^{3+} during the MASS synthesis. As we will show in next section a similar quantum yield can be obtained if MASS-synthesized material is subjected to an additional thermal treatment in a reducing atmosphere.

Persistent Luminescence and Energy Storage Capacity

All the materials were measured following the same procedure described, and the decay curves of the luminance can be observed in **figure 6**. The isothermal decay curves of the luminescence at room temperature for all samples obtained by both MASS and CSS methods behave approximately as a straight line when plotted as a log *I vs.* log *t*.

The total storage capacity, which is related to the absolute number of emitted photons, can be obtained from the luminance decay curves using the equation[37]:

$$N_\gamma = \iint \frac{L(\theta,t)A}{\eta \overline{E}_\gamma} d\Omega dt$$

Where L(θ,t) is the luminance as a function of time and solid angle in cd/m^2, A is the area of the emitting surface, η is the luminous efficacy of the emission spectra in lm/W, and E_γ is the average photon energy.

Overall, the results for the storage capacity show that the MASS-obtained materials have 50, 77, and 31 % higher energy storage than the CSS-obtained ones for the 1, 3, and 10 mole-% of Dy^{3+}, respectively. It can be said that the MASS method shows a moderate improvement when compared to the CSS one, for the different dopant concentration. When high concentration of Dy^{3+} is doped into the crystal (10 mole-%) the higher defects presented in MASS-obtained sample lead to a drop in the storage capacity, in accordance with the previous optical data.

The summarized results of the storage capacity (**Table 1**) show an essential role of the Dy^{3+} co-doping in the storage capacity of the phosphors. The storage capacity increases dramatically when Dy^{3+} concentration in the materials goes from 1 to 3 mole-%. Even though high Dy^{3+} (10 mole-%) concentrations also show a moderate increase in the storage capacity, it is not a linear relation considering the concentration series, mostly because some segregation of Dy^{3+} as observed in SEM-EDX images. Highly concentrated Dy^{3+} areas can also act as a killing centre for the luminescence due to the high number of defects formed by charge compensation effects.

As a matter of comparison, the commercial material Eu^{2+}-doped $Sr_2MgSi_2O_7$ was also analysed by the photon counting and presented a value of 6.52x10^{16} photons/g. Therefore, it is possible to conclude that the MASS synthesis yields efficient storage capacity, and there is still a margin for improvement since the CL showed a significant amount of Eu^{3+} emission in the crystal.

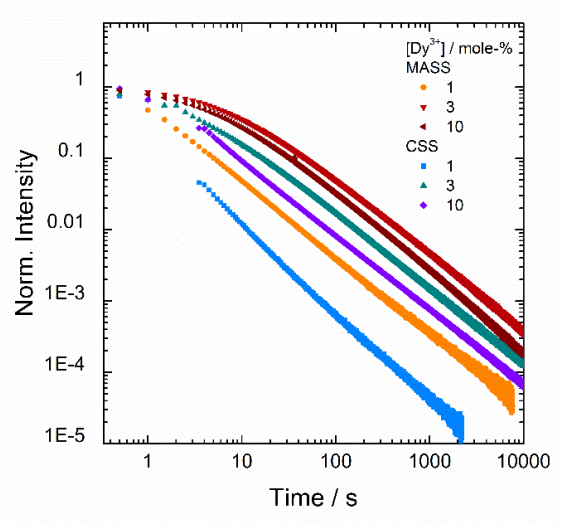

Figure 6. Isothermal luminance decay curves of $Sr_2MgSi_2O_7$:Eu^{2+},Dy^{3+} materials for all studied concentrations, both MASS and CSS methods after excitation for 10 minutes with 375 nm LED.

Table 1. Storage capacity parameter calculated using luminance decay curves of all studied materials.

Dopant: Eu^{2+}/Dy^{3+} (mole-%)		1/1	1/3	1/10
CSS	**Capacity (photons/g)**	1.86x10^{14}	3.15x10^{15}	5.86x10^{15}
MASS	**Capacity (photons/g)**	2.80x10^{14}	5.59x10^{15}	7.01x10^{15}
MASS-Healed	**Capacity (photons/g)**	5.45x10^{15}	9.20 x10^{15}	6.44x10^{15}
COM	**Capacity (photons/g)**	6.52x10^{16}	(Exact concentrations of commercial phosphor are not known)	

Thermoluminescence is particularly useful to assess the mechanism of the trap emptying and the energy of the traps associated with the thermally activated luminescence. In order to investigate the defect structure of the materials prepared by both methods, we registered thermoluminescence glow curves (**Fig. 7**). The experiment was conducted exciting the materials with a 375 nm LED for 10 minutes in order to achieve the saturation of the trapping capacity. All materials were excited at room temperature (293 K), and after the excitation time, the material was cooled to the 213 K. After reaching the desired temperature, the materials were submitted to a constant heating ramp of 0.5 K/s until reaching 473 K. The thermostimulated luminescence (TSL) was recorded using a CCD camera in order to check the emission spectra during the process. The emission spectra for all materials are characteristic for Eu^{2+} emission, with maximum peak and bandwidth analogous to the PL emission (λ_{max}: 470 nm, FWHM: 2300-2500 cm^{-1}).

The materials obtained by both MASS and CSS method present a single glow peak in the temperature interval of -25 to 200 °C. The peak maxima are centred *ca*. 45 °C, allowing efficient persistent luminescence at room temperature. The peak maximum is consistent with other reports in the literature, and it is also showing an optimum range for room temperature PeL.

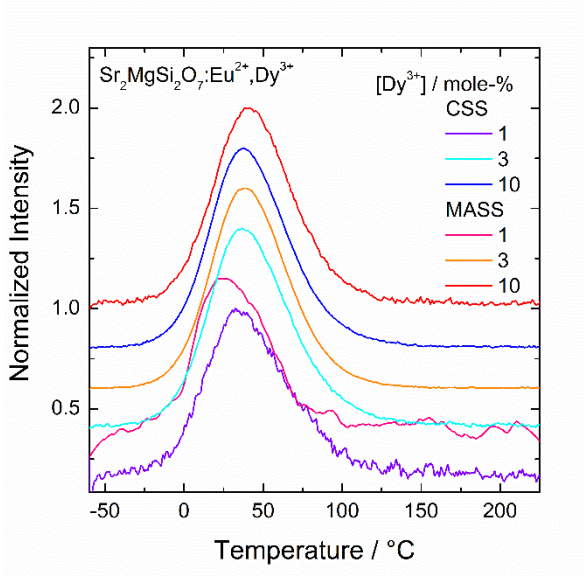

Figure 7. Thermoluminescence glow curves of $Sr_2MgSi_2O_7:Eu^{2+},Dy^{3+}$ materials for all studied concentrations, both MASS and CSS methods.

However, the glow curves present a slight asymmetry there can be an indication of a trap distribution.[51] More experiments are needed to understand the thermoluminescence kinetics of the materials entirely.

It is also clear that the Dy^{3+} co-dopant plays a significant role in the energy storage in the material acting as a centre of electron trapping ($Dy^{3+} + e^-$) or creating more electron deficient traps, such oxygen vacancies. The essential role of the Dy^{3+} in the persistent luminescence of the $Sr_2MgSi_2O_7$ materials are more evident when observing the TL glow curves of the Eu^{2+} single doped materials (not shown here) that have faint intensity.

Reducing post-processing of the MASS-obtained phosphors

After the structural, elemental and spectroscopic characterization of the MASS-obtained samples, it was possible to conclude that the microwave irradiation during the synthesis promoted the following effects: *i*) Higher diffusivity of ions leading to increased rate of the synthesis yielding the $Sr_2MgSi_2O_7$ materials in a mere 25 minutes; *ii*) The increased diffusion also leading to higher incorporation and better distribution of dopants; *iii*) More homogeneously distributed Eu^{2+} ions in the single crystalline phase generating uniform CL emission, at microscopic levels; *iv*) PeL performance with storage capacities higher than to those found with the conventional solid-state methods. However, the SEM-CL showed that part of the europium ions in the $Sr_2MgSi_2O_7$ material are in the trivalent state possibly hindering part of the PL and PeL efficiency. The fact that the method generates only partially reduced materials leads to non-optimal optical properties. Thus, in order to reduce the Eu^{3+} in the lattice, the MASS-obtained phosphors were submitted to an extra heating step, in a tube furnace using dynamic flux of $H_2(10\%)/N_2(90\%)$ gas. Time and temperature were selected in order to prevent excessive crystal growth (30 minutes at 900 °C) using a dynamic gas atmosphere flowing at 200 mL/min. The new post-processed materials are called MASS-Healed.

SEM-CL analysis of the post-treated $Sr_2MgSi_2O_7$ material (**Fig. 8**) doped with the 1 mole-% of both Eu and Dy showed a successful reduction of Eu^{3+} to Eu^{2+} in the selected area of analysis. Most of the examined area is composed by the CL emission spectra centred at 468 nm attributed to the Eu^{2+} already described in previous sections. Also, Dy^{3+} emission is still observed as expected due to the high energy excitation source. In the obtained image, small inter grain impurities are also present. Nevertheless, the material is outstandingly homogeneous throughout the analysed area with constant FWHM and peak wavelength position for the CL emission spectra.

The performance of the optical properties showed a considerable increase with a higher quantum yield (35 %) and higher fractions of absorbed light compared to the non-healed material. After post-processing, the luminescence quantum yield of the materials obtained by the two methods (CSS and MASS) is comparable. This leads to values of quantum yield close to the observed in the literature (40%) and the commercial materials (45 %).[49]

When comparing the decay curves of the materials with the same dopant concentration, obtained by the different methods, it is easily seen the superiority of the MASS-healed samples **(Figure 9a)**. However, the improvement seems to be dependent on the Dy concentration; the lower the concentration the higher the improvement. When doped with 10 mole-% of Dy the improvement due to the reduction step are negligible (**Table 1**). For low Dy^{3+} concentrations (1 mole-%) the change is quite spectacular showing and improvement of 20 times higher than the non-healed sample and 30 times higher than the CSS one.

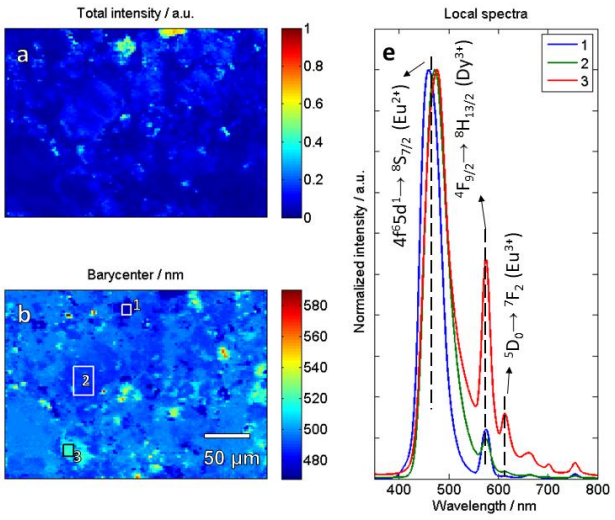

Figure 8. SEM-CL hyperspectral image of the $Sr_2MgSi_2O_7:Eu^{2+}(1\%),Dy^{3+}(1\%)$ material obtained by MASS after healing post-processing in reducing atmosphere.

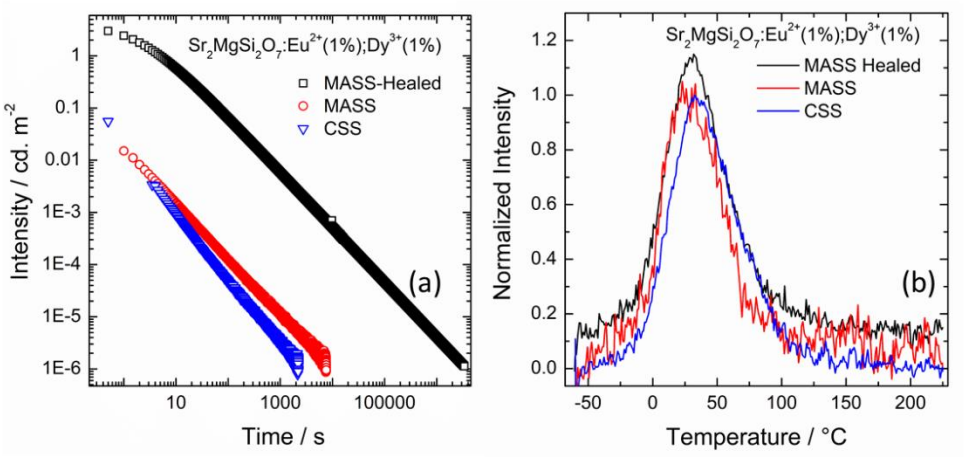

Figure 9. Comparison of the isothermal decay of the luminescence (a) an the thermoluminescence glow curves (b) for the $Sr_2MgSi_2O_7$:Eu,Dy (1 mole-%) materials obtained by CSS, MASS (before and after reduction step) methods.

When comparing the thermoluminescence glow curves for the materials with the same dopant concentration, obtained by the different methods (**Fig. 9b**) it is possible to confirm that the nature of the traps is the same in all samples. The glow peak maxima registered for the healed phosphors are 31 (1% Dy^{3+}), 45 (3% Dy^{3+}), and 40 °C (10% Dy^{3+}), in comparison with 26, 38 and 40 °C for the samples before the reduction indicating the same defect structure on both materials. Also, the CIE color diagram (**Fig. S5**) showed that the MASS emission sample is more dislocated towards the red; however, after the reduction step the colour coordinates shifts towards the blue region, closer to the CSS sample.

The excellent performance is attributed to the combination of the well-distributed Eu^{2+} ions in a chemically homogeneous host yielding homogeneous PL emission throughout the crystal with a higher density of traps at the investigated temperature. Both effects are related to increased diffusion enhanced by the microwave irradiation during the synthesis.

Conclusion

High-quality $Sr_2MgSi_2O_7$:Eu^{2+},Dy^{3+} persistent luminescence materials were obtained by a microwave-assisted solid-state method. The analysis of the structure showed that the MASS method yields highly crystalline Sr-åkermanite materials in 22-25 minutes, in a 900 to 1000 W microwave irradiation regime. Rietveld refinements showed better incorporation of Dy^{3+} in the MASS-obtained materials in comparison with the CSS-one. In terms of chemical yield, the MASS method is a cost-effective, efficient method to obtain $Sr_2MgSi_2O_7$ materials with comparable impurity levels as CSS-obtained ones. Hyperspectral imaging of the MASS materials confirmed a high homogeneous local CL emission consistent with a high chemical homogeneity in the crystals attributed to microwave-enhanced diffusion of the species during the synthesis. MASS-obtained materials showed from 30 to 77% higher storage capacity than the CSS materials. However, after an additional heating step to adequately reduce the Eu^{3+} to Eu^{2+} of the MASS-obtained materials, the storage capacity increased 10-fold. The obtained values are comparable to the commercial materials measured by the same method. These data lead to the conclusion that the MASS method, in combination with additional short reducing step, achieved a high-quality persistent luminescence material, with a high-homogeneous local structure, and superior storage capacity performance. Also, the novel strategy could be used to obtain a myriad of inorganic luminescent materials in order to achieve high optical performance.

ACKNOWLEDGMENT

The author José Miranda de Carvalho thanks FAPESP for the financial support through the Project BEPE n° 2018/09403-4, and Project n° 2017/05195-5. The author JMC also thanks Profª Márcia C.A. Fantini for the XRD and Dr. Jonas Joos for rare earth spectroscopy discussions. Olivier Janssen is acknowledged for the XRD and SEM imaging assistance. David Van der Heggen is grateful to the UGent Special Research Fund (BOF) for financial support (BOF16/DOC/327)

REFERENCES

1 N. Nitta, F. Wu, J. T. Lee and G. Yushin, *Mater. Today*, 2015, **18**, 252–264.

2 C. L. Pint, N. W. Nicholas, S. Xu, Z. Sun, J. M. Tour, H. K. Schmidt, R. G. Gordon and R. H. Hauge, *Carbon N. Y.*, 2011, **49**, 4890–4897.

3 S. G. Kim, J. S. Han, H. Kim, S. Y. Kim and H. W. Jang, *Adv. Mater.*, 2018, **1800457**, 1–30.

4 Y. H. Kim, P. Arunkumar, B. Y. Kim, S. Unithrattil, E. Kim, S. H. Moon, J. Y. Hyun, K. H. Kim, D. Lee, J. S. Lee and W. Bin Im, *Nat. Mater.*, 2017, **16**, 543–550.

5 S. Nakamura, T. Mukai and M. Senoh, *Jpn. J. Appl. Phys.*, 1991, **30**, L 1998-L 2001.
6 E. F. Schubert and J. K. Kim, *Science.*, 2005, **308**, 1274–1278.
7 A. Birkel, K. A. Denault, N. C. George, C. E. Doll, B. Héry, A. A. Mikhailovsky, C. S. Birkel, B. C. Hong and R. Seshadri, *Chem. Mater.*, 2012, **24**, 1198–1204.
8 P. F. Smet and J. J. Joos, *Nat. Mater.*, 2017, **16**, 500–501.
9 Y. Liang, F. Liu, Y. Chen, K. Sun and Z. Pan, *Dalt. Trans.*, 2016, **45**, 1322–1326.
10 Y. Liang, F. Liu, Y. Chen, X. Wang, K. Sun and Z. Pan, *Dalt. Trans.*, 2017, **46**, 11149–11153.
11 E. Glais, M. Pellerin, V. Castaing, D. Alloyeau, N. Touati, B. Viana and C. Chanéac, *RSC Adv.*, 2018, **8**, 41767–41774.
12 S. K. Singh, *RSC Adv.*, 2014, **4**, 58674–58698.
13 J. Wang, Q. Ma, Y. Wang, H. Shen and Q. Yuan, *Nanoscale*, 2017, **9**, 6204–6218.
14 K. Fiaczyk, A. J. Wojtowicz and E. Zych, *J. Phys. Chem. C*, 2015, **119**, 5026–5032.
15 Y. Xu and D. Chen, *Ceram. Int.*, 2008, **34**, 2117–2120.
16 T. Peng, L. Huajun, H. Yang and C. Yan, *Mater. Chem. Phys.*, 2004, **85**, 68–72.
17 K. J. Rao, B. Vaidhyanathan, M. Ganguli and P. A. Ramakrishnan, *Chem. Mater.*, 1999, **11**, 882–895.
18 H. J. Kitchen, S. R. Vallance, J. L. Kennedy, N. Tapia-Ruiz, L. Carassiti, A. Harrison, A. G. Whittaker, T. D. Drysdale, S. W. Kingman and D. H. Gregory, *Chem. Rev.*, 2014, **114**, 1170–1206.
19 C. C. S. Pedroso, J. M. Carvalho, L. C. V. Rodrigues, J. Hölsä and H. F. Brito, *ACS Appl. Mater. Interfaces*, 2016, **8**, 19593–19604.
20 R. Yuvasravana, P. P. George and N. Devanna, *Mater. Today Proc.*, 2017, **4**, 10664–10671.
21 L. Pan, S. Liu, X. Zhang, O. Oderinde, F. Yao and G. Fu, *J. Alloys Compd.*, 2018, **737**, 39–45.
22 J. Miranda De Carvalho, C. C. S. Pedroso, I. P. Machado, J. Hölsä, L. C. V. Rodrigues, P. Głuchowski, M. Lastusaari and H. F. Brito, *J. Mater. Chem. C*, 2018, **6**, 8897–8905.
23 J. M. Carvalho, I. Norrbo, R. A. Ando, H. F. Brito, M. C. A. Fantini and M. Lastusaari, *Chem. Commun.*, 2018, **54**, 7326–7329.
24 A. G. Whittaker, *Chem. Mater.*, 2005, **17**, 3426–3432.
25 L. I. D. J. Martin, D. Poelman, P. F. Smet and J. J. Joos, *ECS J. Solid State Sci. Technol.*, 2018, **7**, R3052–R3056.
26 K. Van den Eeckhout, P. F. Smet and D. Poelman, *Materials (Basel).*, 2010, **3**, 2536–2566.
27 H. Sun, L. Pan, G. Zhu, X. Piao, L. Zhang and Z. Sun, *Dalt. Trans.*, 2014, **43**, 14936–14941.
28 F. Chi, X. Wei, B. Jiang, Y. Chen, C. Duan and M. Yin, *Dalt. Trans.*, 2018, **47**, 1303–1311.
29 K. Ikegaya, S. Yamada and K. Shinozaki, *Dalt. Trans.*, 2019, **48**, 6746–6756.
30 H. F. Brito, J. Hölsä, T. Laamanen, M. Lastusaari, M. Malkamäki and L. C. V Rodrigues, *Opt. Mater. Express*, 2012, **2**, 371–381.
31 I. Norrbo, J. M. Carvalho, P. Laukkanen, J. Mäkelä, F. Mamedov, M. Peurla, H. Helminen, S. Pihlasalo, H. Härmä and J. Sinkkonen, *Adv. Funct. Mater.*, 2017, **27**, 1–9.
32 J. Xu and S. Tanabe, *J. Lumin.*, 2019, **205**, 581–620.
33 I. P. Sahu, D. P. Bisen, N. Brahme and M. Ganjir, *Luminescence*, 2015, **30**, 1318–1325.
34 Y. Lin, Z. Tang, Z. Zhang, X. Wang and J. Zhang, *J. Mater. Sci. Lett.*, 2001, **20**, 1505–1506.
35 J. Lasri, P. D. Ramesh and L. Schächter, *J. Am. Ceram. Soc.*, 2000, **83**, 1465–1468.
36 B. H. Toby, *J. Appl. Crystallogr.*, 2001, **34**, 210–213.
37 D. Van der Heggen, J. J. Joos, D. C. Rodríguez Burbano, J. A. Capobianco and P. F. Smet, *Materials (Basel).*, 2017, **10**, 1–13.
38 M. Ardit, M. Dondi, M. Merlini and G. Cruciani, *Phys. Chem. Miner.*, 2012, **39**, 199–211.
39 R. D. Shannon, *Acta Crystallogr. Sect. A*, 1976, **32**, 751–767.
40 A. Denton, *Phys. Rev. A*, 1991, **43**, 3161–3164.
41 M. Ardit, M. Dondi, I. National, M. Merlini and G. Cruciani, *Phys. Chem. Miner.*, 2012, **39**, 199–211.
42 J. Hölsä, T. Laamanen, M. Lastusaari and P. Novák, *J. Rare Earths*, 2011, **29**, 1130–1136.
43 H. Duan, Y. Z. Dong, Y. Huang, Y. H. Hu and X. S. Chen, *Phys. Lett. Sect. A Gen. At. Solid State Phys.*, 2016, **380**, 1056–1062.
44 M. Kahlweit, *Adv. Colloid Interface Sci.*, 1975, **5**, 1–35.
45 M. Zhao, M. Johnson, W. He, G. Li, C. Zhao, L. Yu, J. Huang and H. Zhu, *Materials (Basel).*, 2018, **11**, 1–14.
46 M. Ding, C. Lu, Y. Ni and Z. Xu, *Chem. Eng. J.*, 2014, **241**, 477–484.
47 J. J. Joos, L. Seijo and Z. Barandiaran, *J. Phys. Chem. Lett.*, 2019, **10**, 1581–1586.
48 S. H. M. Poort, H. M. Reijnhoudt, H. G. T. Van Der Kuip and G. Blasse, *J. Alloys Compd.*, 1996, **241**, 75–81.
49 G. Blasse, W. L. Wanmaker, J. W. Vrugt and A. Bril, *Philips Res. Repts*, 1968, **23**, 189–200.
50 D. Van der Heggen, J. Joos and P. F. Smet, *ACS Photonics*, 2018, **5**, 4529–4537.
51 K. Van Den Eeckhout, A. J. J. Bos, D. Poelman and P. F. Smet, *Phys. Rev. B*, 2013, **87**, 045126.
52 K. Momma and F. Izumi, *J. Appl. Crystallogr.*, 2011, **44**, 1272–1276.

